The interpretation of X-ray Computed Microtomography images of rocks as an application of volume image processing and analysis

Kaczmarczyk J., Dohnalik M., Zalewska J.
Oil and Gas Institute
Well Logging Department
ul. Lubicz 25 A
Poland, 31-503 Kraków
jan.kaczmarczyk@inig.pl

Cnudde, V.
The Center for X-Ray Tomography
Department of Geology and Soil Science
Ghent University
Krigslaan 281, S8
Belgium,9000 Ghent

ABSTRACT

X-ray computed microtomography (CMT) is a non-destructive method of investigating internal structure of examined objects. During the reconstruction of CMT measurement data, large volume images are generated. Therefore, the image processing and analysis are very important steps in CMT data interpretation.

The first step in analyzing the rocks is image segmentation. The differences in density are shown on the reconstructed image as the differences in gray level of voxel, so the proper threshold operation must be carried out. As a result, the different mineral phases and pores can be separated at the image.

Segmented and binarized image is the base for further operations which depend on the aim of research.

Numerical analysis gives information about the pore shapes and volumes as well as connections between pores in the pore network.

The image may also be used in numerical physics simulation (for example fluid flow simulation), but before that it has to be filtered and resampled. These operations are very important, because if performed poorly, they may lead to rupture the pore network.

The aim of this paper is to present authors' methodology of CMT image processing and analysis and to show problems occurring during these processes. The image processing of two rock samples CMT image will be presented.

Keywords

tomography, CMT, volume image, segmentation, image analysis

1. INTRODUCTION

1.1 X-ray Computed Microtomography

The foundations of microtomography were developed shortly after discovering the X-rays by Wilhelm Röntgen. In 1917 Johann Radon proposed the theory of computed tomography (CT)[Hsi03, Rec08] - mathematical reconstruction of object's internal structure based on infinite number of its X-ray projections. On the basis of this theory EMI Scanner - the first medical CT scanner - was used to brain imaging in 1968. In 1970s medical scanners were used to rock cores imaging. Due to relatively low resolution (in order of mm) of these scanners, in 1990s the computed microtomography (CMT, micro-CT) systems were developed[Cnu06]. These systems, with resolution down to 0.4 μm, have a different geometry, with rotating examined object and stationary X-ray source-detector line. Additionally, the X-ray spot and detector pixel were reduced in order to increase resolution[Ket01, Kac08].

Scheme of CMT measurement and data processing was shown in figure 1[Fer07].

Every tomography measurement includes two steps: the data acquisition and the image reconstruction. During the data acquisition the set of 2D object's projections are collected. The gray level of every point of projection is determined by the Beer's law for complex materials[Ket01]:

$$I = I_0 e^{-\Sigma_i(\mu_i \cdot l_i)}, \quad (1.1)$$

where the I_0 is the initial X-ray intensity, I - beam intensity after passing the object, μ_i - linear attenuation coefficient and l_i - linear extent of i material. At the reconstruction step the internal structure of the examined object is calculated as a superposition of recorded projections.

After reconstruction process, the 3D gray-scale structure of object is obtained. The gray level of each point is proportional to linear attenuation coefficient μ_i of the material and it is (in case of X-rays) proportional to the material's density. The brighter voxel, the higher density of material in the volume element of object.

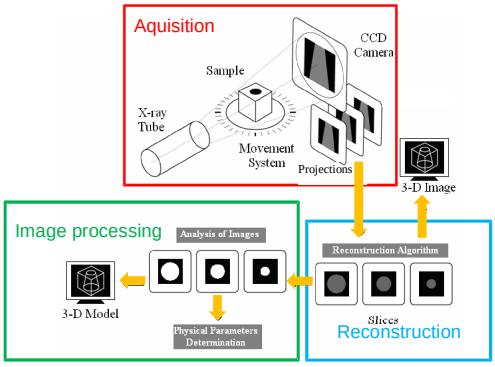

Figure 1. Principle of CMT measurement and data processing [Fer07]

1.2 Geophysical Aspect

Porosity and permeability are important properties of reservoir rocks[Sal03]. Porosity (ε) is the percentage of the sample's volume that is occupied by air (and may be occupied by some fluid):

$$\varepsilon = \frac{V_a}{V_s} = \frac{V_a}{V_r + V_a}, \quad (1.2)$$

where V_a is a volume occupied by air, V_s - sample's volume, and V_r - a volume occupied by a rock matrix. It is measured by gas absorption, mercury porosimetry or density measurements. Permeability (κ) is the ability of the material (e.g. rock) to transport fluids[Har00]. It is determined experimentally in the permeability test with use of Darcy's law:

$$u = -\frac{\kappa}{\eta} \nabla p, \quad (1.3)$$

where u is velocity field, η - dynamic viscosity of fluid, and ∇p - the gradient of pressure at the examined sample. The permeability may also be calculated with the use of microscopic properties of the examined material as:

$$\kappa = C \cdot d^2, \quad (1.4)$$

where C is the dimensionless constant describing pores geometry and d is the average effective pore diameter.

Both properties may be calculated from CMT measurements[Nar09], but the acquired image has to be treated in specific way.

1.3 Image Processing

As a result of image reconstruction, the volume gray scale image is obtained. This is rather big data set (about 10 GB per every measurement), so every treatment which reduces its volume without loss of quality is desirable. In fact, the image processing depends on the aim of CMT imaging.

The first and the most important step of CMT image analysis is image segmentation. The initial gray-scale image must be divided into different phases - e.g. pores and different rock phases in case of rock's analysis. Three different segmentation techniques will be described later.

Analysis of CMT image requires an image containing a large amount of details. Fortunately, image analysis is not CPU and memory consuming process and image simplification is not required.

Dues to large volume of CMT data, for fluid flow simulation it is necessary to reduce the volume of reconstructed image. This may be done by pores' extraction and image resampling. The problem is the loss of information during image simplification. In the extreme cases image processing may lead to the rupture of the pores' connections, which results in producing false results of the simulation.

1.4 Image Analysis

One of CMT's advantages is the ability to show the real pore's shape and size (which is impossible with the use of conventional methods), so it is necessary to find the way of analyzing this features of the segmented image.

Pore's size may be easily described after its labeling. In this process every group of connected (in determined neighborhood) voxels (which is equivalent to pore) is labeled as another object and has a different gray level assigned. Then, properties of every object (as size or shape) may be easily described.

1.4 Scope of research

The aim of this article is to present CMT image processing and analysis. Analysis becomes a standard method of rock's characterization during mine survey. Image processing is an important step of

preparing CMT-based fluid flow simulation, which is the current topic of the authors' studies.

2. EXPERIMENTAL

2.1 CMT Equipment

The measurements were performed on X-Tek Benchtop CT-160Xi microtomograph. The current at Cu lamp was 60 μA and voltage was 110 kV. The Varian PaxScan 2520V detector was used. The rock samples were in the form of core with a diameter of 10 mm. During every scan about 3000 projections were made with step about 0.12°.

2.2 Examined samples

To present the application of CMT measurements, two rock samples were chosen. The first one, sample 1, was a rock core excavated from oil-bearing area and its porosity (calculated from density measurements) was 29,45 %. The second one, sample 2, was a rock core with porosity 4,90 %.

Examined image size was 1000×1000×400 voxels in case of sample 1 and 556×951×552 voxels in case of sample 2.

2.3 Data Processing

The internal structure of the examined rocks was reconstructed with the use of Benchtop CT-Pro Client software with Feldkamp's algorithm[Fel84] for cone-beam experiment. The voxel size of reconstructed image was 5.8×5.8×5.8 μm^3.

ImageJ[ImJ] was used for the histogram calculation.

VSG Avizo 6[Avi] software was used for the image segmentation and visualizations. Images were filtered by unsharp masking, segmented with the use of the threshold tool, and then islands (up to 2 voxels, 25 %) were removed. Before visualization, the images were resampled by factor 2. The surfaces were generated with constrained smoothing.

MAVI 1.3.1[MAV] (Modular Algorithms for Volume Images) software was used for pores' size analysis and pores extraction. The sample was binarized, labeled at neighborhood 26/8 and then the objects' features were calculated. The image was also divided into 6 pore classes according to their volume (table 1).

3. SEGMENTATION

3.1 Thresholding Techniques

Three different threshold techniques developed on the basis of [Mor00] were used.

First, threshold along boundaries, was used for segmenting CMT picture into pore network and rock matrix. On the histogram the minimum was found and this gray value was marked as Th_{min}. Next, the points with gray value Th_{min}±5 were selected on the analyzed image (and the boundary between pore and rock was marked). In the neighborhood-8 of 10 of these points, points with gray value of Th_{min}+20 were selected. The average of averages of all the selected points gray levels was adopted as threshold value (Th_B).

class	volume /voxels	colour
I	1-9	Yellow
II	10-99	Blue
III	100-999	Red
IV	1000-9999	Green
V	10000-99999	White
VI	> 100000	violet

Table 1. Pore's classes and colours of its visualization.

The phase-mean threshold was used for phase location analysis. The number of phases on the image was estimated visually. Then 10 points from every phase was randomly selected and the G_{phn} were calculated as the average of gray value of the points belonging to the n-phase. The threshold Th_{ij} (i and j are phases numbers) between the phases was calculated as the average of G_{phn}'s for the phases with similar gray values.

The histogram threshold was calculated (with Fityk[Fit] software) by fitting n Gaussian curves (where n is the number of rock's phases + 1) to the histogram of the CMT image. Threshold value (Th_h) was taken at the first curves intersection (figure 2).

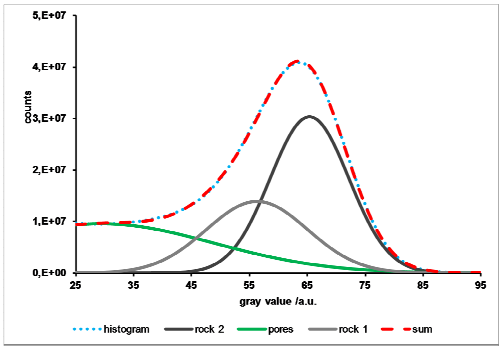

(a)

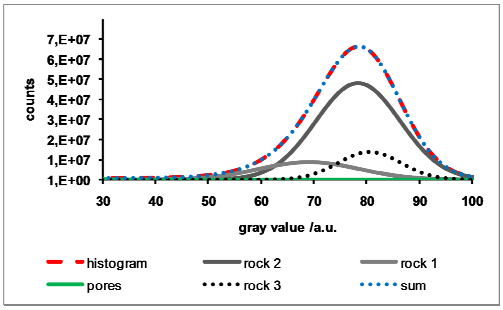

(b)

Figure 2. Histogram deconvolution (a) sample 1, 3 Gaussian curves, (b) sample 2, 4 Gaussian curves.

Threshold values estimated with different methods was shown in table 2.

sample	threshold method	threshold
1	boundary	40
	histogram	45
	phase-mean	35
2	boundary	40
	histogram	47
	phase-mean	39

Table 2. Values of threshold between pore and rock phase while using different threshold techniques.

The result of these three methods on image segmentation was shown in figures 3 and 4.

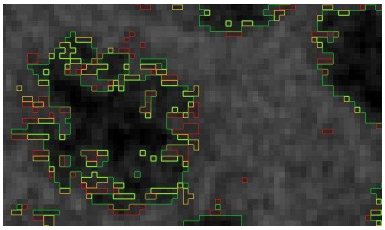

Figure 3. Sample 1 - the pore's border for three different threshold methods; yellow line - the threshold along boundaries, red - the histogram threshold, green - the phase-mean threshold.

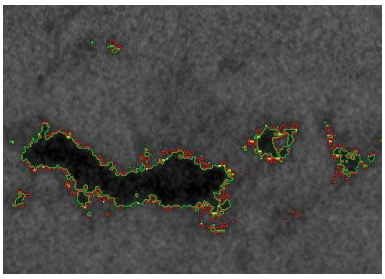

Figure 4. Sample 2 - the pore's border for three different threshold methods; yellow line - the threshold along boundaries, red - the histogram threshold, green - the phase-mean threshold.

As it was shown in figures 3 and 4, histogram threshold technique may result in shifting threshold (between pores and rock) gray value toward higher values.

3.2 The effect of Segmentation on Porosity

All of described thresholding techniques lead to calculate porosity of the examined sample as:

$$\epsilon = \frac{n_p}{\sum_i n_i} \cdot 100\%, \qquad (3.1)$$

where n_p is number of voxels assigned to pore layer and $\underline{n_i}$ is number of voxels assigned to *i*-layer.

Table 3 shows the porosity values of samples 1 and 2 while using different threshold techniques.

sample	threshold method	porosity /%
1	boundary	27.2
	histogram	31.2
	phase-mean	23.7
2	boundary	2.0
	histogram	2.6
	phase-mean	1.9

Table 3. Porosity calculated with the use of equation (3.1) while using different threshold techniques.

Porosity values estimated by CMT measurements are generally lower than porosity values calculated with density measurements (sample 1 - 29,45 %, sample 2 - 4,90 %). This is due to the measurement resolution - while using CMT equipment it was impossible to notice pores with volume of less than 195 μm^3.

It is worth noticing that histogram thresholding in case of sample 1 gave the porosity value higher than real porosity of examined sample. It proves that using described simple histogram segmentation technique is not accurate for rock's examining

Two other thresholding techniques gave reliable porosity values. Thresholding along boundaries leads to higher values, closer to the real porosity. Therefore, this technique was recognized as the best for rock's porosity evaluation.

3.3 Phase Location Analysis

The gray value of voxel on the reconstructed image is determined by attenuation coefficient of material and it is proportional to the material's density. Therefore the voxel's gray level may lead to phase-segmentation of reconstructed image. Every separated phase has a significantly different density. These phases may (but need not) correspond to mineral phases present in the examined sample.

The phase location analysis was performed only with the use of phase-mean thresholding. With the use of thresholding along boundaries it was impossible to determine more than two (pores and rock) phases. The histogram thresholding technique was rejected during porosity examining.

In sample 1 three phases (pores and two rock phases) were recognized (figure 5). In sample 2 four phases were selected (figure 6). Used threshold values were shown in table 4.

The volume fraction (f_i) of each phase was calculated as:

$$f_i = \frac{n_i}{\Sigma_j n_j}, \qquad (3.2)$$

where n_i is number of voxels assigned to i-phase layer and n_j is number of voxels assigned to j-phase (i and j refer to rock layers only).

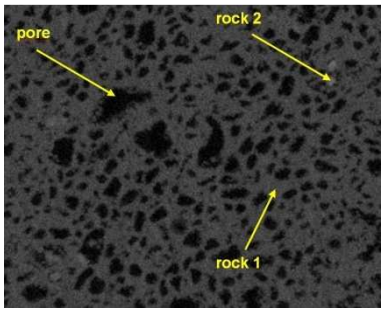

Figure 5. Pores and two different rock phases recognized in sample 1.

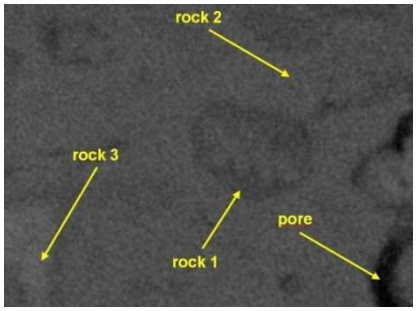

Figure 6. Pores and three different rock phases recognized in sample 2.

Sample	phase	gray value
1	pores	< 35
	rock 1	35-78
	rock 2	> 78
2	pores	< 39
	rock 1	40-72
	rock 2	72-84
	rock 3	> 84

Table 4. The gray values for each recognized phase in samples 1 and 2.

Figures 7 and 8 and table 5 present the results of phase location analysis of sample 1 and 2.

As it was shown in figure 5 and in table 5, the most volume in sample 1 is occupied by a phase with lower density. Phase rock 2, with higher density, is located in the clusters scattered through the bulk of the sample. The pore space in sample 1 is uniformly distributed through the sample's space.

In sample 2, as it was presented in figure 8 and in table 5, the main phase (55 %) is rock phase 2 (with medium density). It is uniformly distributed in sample's space. The densest phase, rock 3, is located mainly at the top of the sample. The pore space in sample 2 is condensed in the crack in the middle of the sample.

Sample	phase	volume fraction /%
1	rock 1	95.3
	rock 2	4.7
2	rock 1	28.2
	rock 2	55.1
	rock 3	16.7

Table 5. Participation of rock phases of different density in sample's rock skeleton.

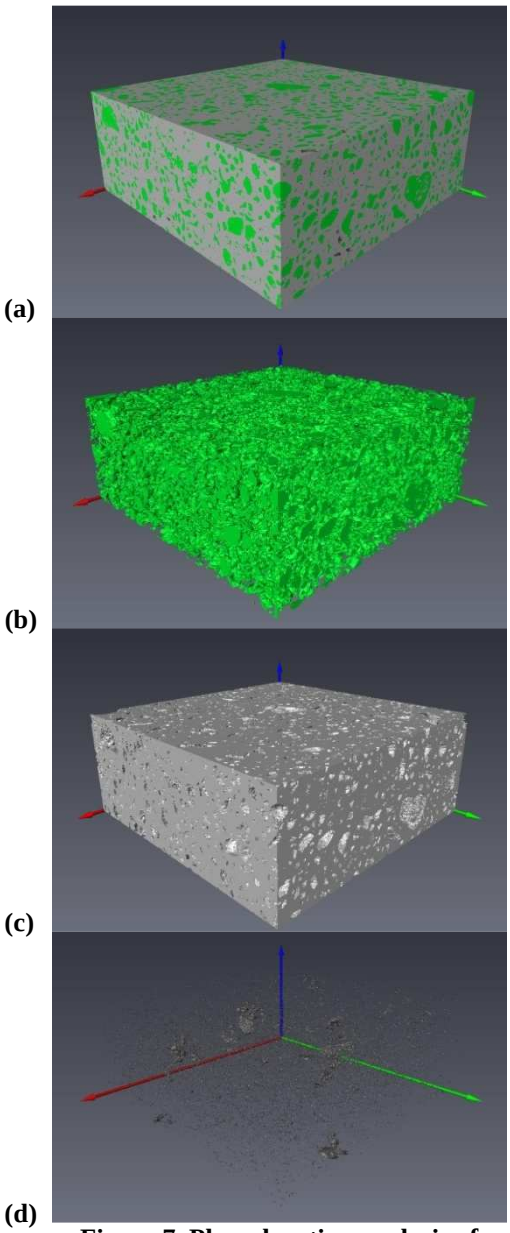

Figure 7. Phase location analysis of sample 1: (a) whole sample with 3 phases, (b) pore space, (c) rock 1 phase, (d) rock 2 phase. Phase's 1 density is higher than density of phase 2.

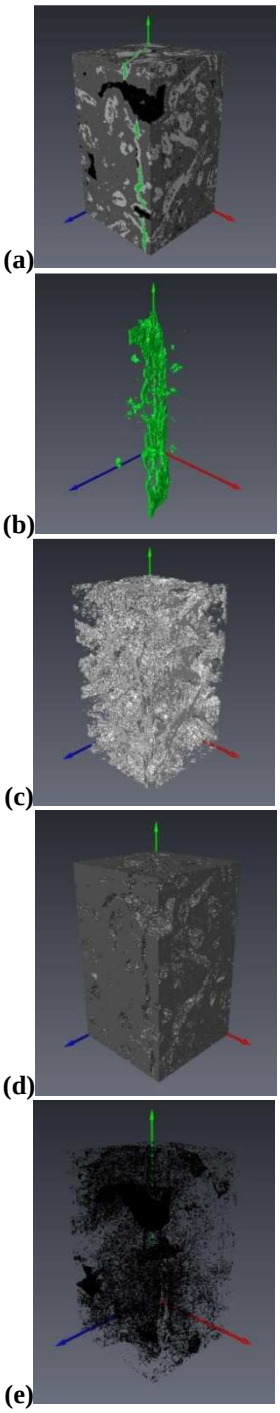

Figure 8. Phase localization in sample 2: (a) whole sample, (b) pore space, (c) rock 1, (d) rock 2, (e) rock 3; the darker color, the denser rock phase.

4. IMAGE ANALYSIS

4.1 Pore Size Distribution

The segmented (with the use of threshold along boundaries) image was saved as RAW data and the pores' layer was labeled (with use of neighborhood 26/8) in MAVI software. Then objects' features were calculated and the pores were divided into classes according to their volume (table 1). Every class was saved in another RAW file and visualized. The objects' features were exported to CSV file and the pore size distribution graph was plotted for every sample.

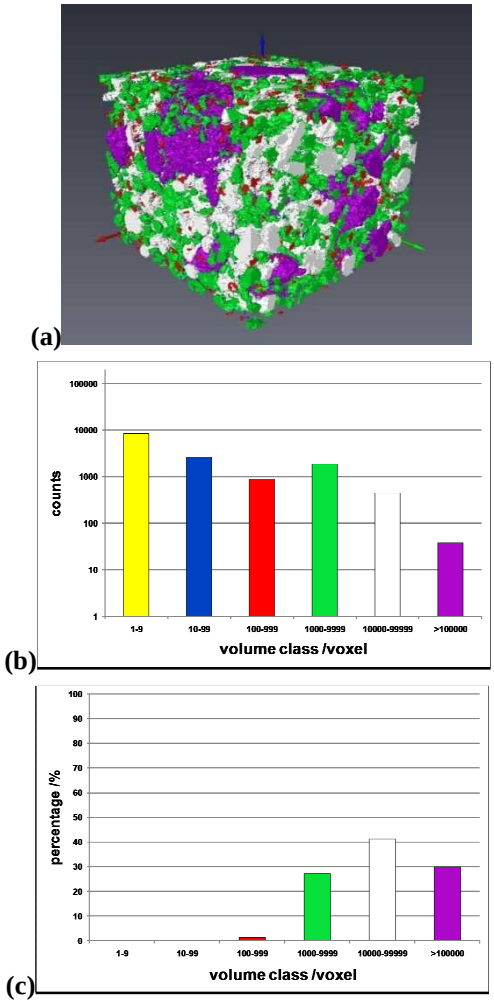

Figure 9. Pore size distribution of sample 1 (cropped to 500x500x400 voxels). (a) visualization of pores location, (b) pores quantitative distribution, (c) percentage (v/v) distribution.

Sample 1, because of its volume, was cropped to 500x500x400 voxels (selected region was located in the middle of sample). The pore's size distribution analysis of sample 1 was presented in figure 9. The cropped fragment of sample 1 contained 14198 objects (pores). As it was shown in figure 9a, they were uniformly distributed at whole sample volume. Figures 9b and 9c shown, that the cropped volume of sample 1 contains about 40 pores with volume above 100000 voxels, but the higher contribution of pore space volume belongs to pore with volume 10000-99999 voxels.

Pore size distribution analysis of sample 2 was presented in figure 10. The distribution of pores' size in sample 2 is quite different than in sample 1. Sample 2 contains only 1 pore with size beyond

100000 voxels, but it makes about 90 % of pore space volume. As it was written above, the pores are concentrated around the crack in the middle of the sample.

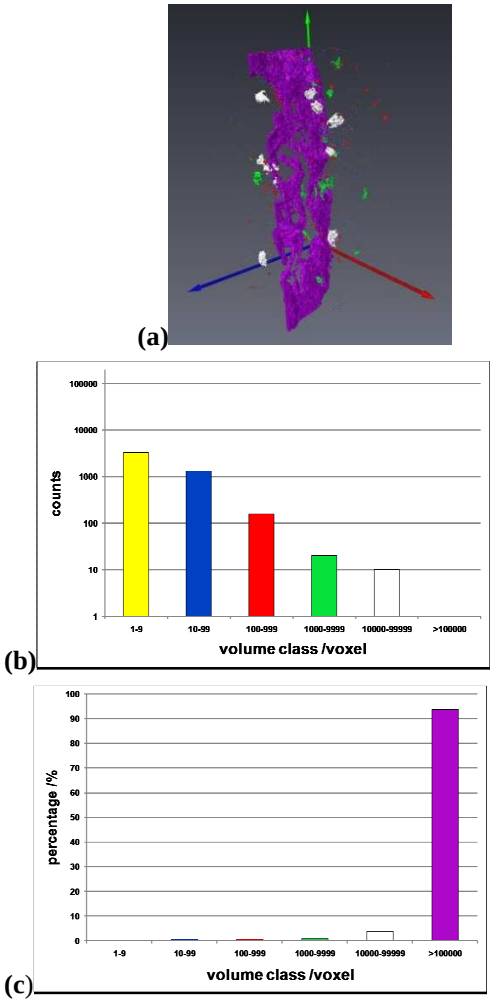

Figure 10. Pore size distribution of sample 2. (a) visualization of pores location, (b) pores quantitative distribution, (c) percentage (v/v) distribution.

5. PREPARING DATA FOR FLUID FLOW SIMULATION

Tortuosity analysis proves that sample 1 has no connections in pore space between opposite sides of the sample. Sample 2 has a channels with average tortuosity 1.1 in y direction (green axis in figures) and 1.4 in z direction (blue axis). Therefore only sample 2 was taken into consideration for fluid flow simulation.

In the fluid transport phenomena only pores with the highest volume participate, so the first step in image simplifying was pores extraction. A pore with volume of 5407370 voxels (the crack) was extracted from sample 2 and the image was saved in the RAW data file. Except this pore, sample 2 has no connections between pores, so the other pores do not participate in fluid transport in this sample.

The extracted pore was labeled and visualized with the use of Avizo software. Next the labeled sample was linearly resampled by factor 2, 4, 6, 8, and 10. The results of resampling were shown in figure 11 and 12.

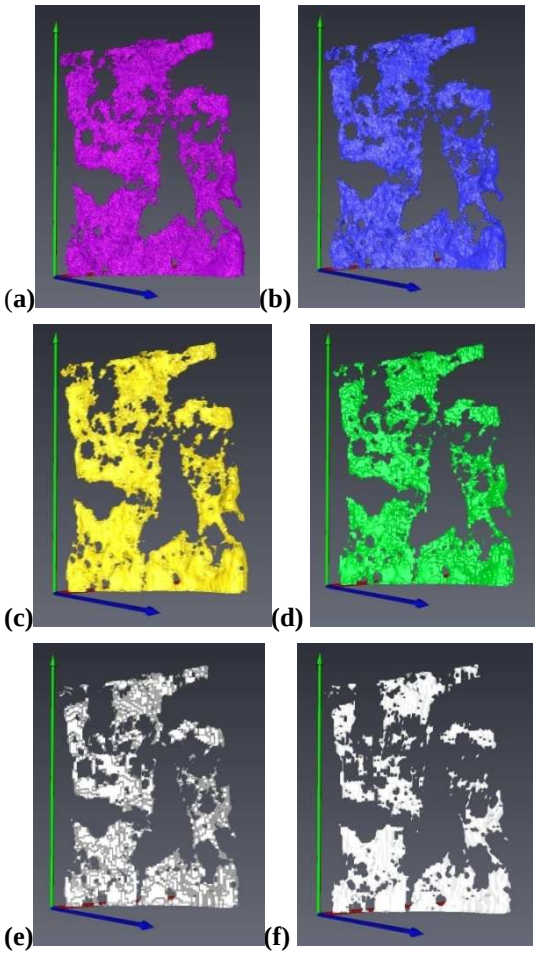

Figure 11. Crack seen in sample 2 (a) without resampling and resampled by factor (b) 2, (c) 4, (d) 6, (e) 8, (f) 10.

Resampling has noticeable effect on pores connections. The tortuosity analysis proves that resampling by factor 10 resulted in breaking all connections in y direction. In figure 12 the input crack and the crack resampled by factor 8 were compared and the visible ruptures in the pore network were marked.

It should be noticed that MAVI software takes account of neighborhood 26 of each voxel for tortuosity calculation. FEM calculation software COMSOL [Com] takes into account neighborhood 6. This means that the rupture of pore network during image resampling may have occurred earlier than it was detected in MAVI software.

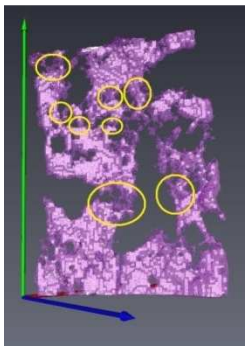

Figure 12. Comparision of figure 11(a) and 11(e). The visible interruptions of pore network were marked.

This example shows that preparing CMT image for fluid flow simulation is not a simple task. Connections between pores have a decisive impact on fluid flow in porous media, so they cannot be interrupted during the image processing.

6. Conclusions

CMT images of two rock samples with different porosity were processed and analyzed.

Three threshold methods were tested. Threshold based on the histogram deconvolution was rejected because porosity estimated with this method was higher than physical porosity of the sample. The best of examined segmentation methods for rock's porosity analysis was threshold along boundaries.

Phase analysis of the samples was executed with the use of phase-mean threshold. The sample was divided into phases with different density. The development of this method provides a basis for detection of different mineral phases in the sample with the use of CMT method.

While preparing sample to fluid flow simulation, the connections between pores were interrupted when the sample was resampled. Sample 2 after resampling by factor 10 has a dimensions 56×95×55 voxels. It is acceptable, but the simulation takes a long time on computer with 8-cores processor. Thus some better way of image processing should be sought.

Optimization of image processing for simulation will be the aim of the further authors' research.

7. REFERENCES

[Avi] VSG Avizo 6.1, http://www.vsg3d.com/vsg_prod_avizo_overview.php

[Cnu06] Cnuddle V., Masschaele B., Dierick M., Vlassenbroeck J., Van Hoorebeke L., Jacobs P., Recent progress in X-ray CT as a geosciences tool, App. Geochem. 21, pp. 826-832, 2006.

[COM] COMSOL Multiphysics 3.5a, http://www.comsol.com/products/multiphysics/

[Fel84] Feldkamp L. A., Davic L. C., Kress J. W., Practical cone-beam algorithm, . Opt. Soc. Am. A Vol. 1 No. 6, pp. 612-619, 1984.

[Fer07] Fernandes J. S., Appoloni C. R., Moreira A. C., Fernandes C. P., Porosity and pore size distribution determination of tumblagooda formation sandstone by X-Ray Microtomography, 2007 International Nuclear Atlantic Conference INAC 2007.

[Fit] Fityk 0.8.9, http://www.unipress.waw.pl/fityk/

[Har00] Harrison J., Hudson J., Engineering Rock Mechanism, Part 2, chapter 9: Porosity, pp.141-159, Elsevier 2000.

[Hsi03] Hsieh J., Computed Tomography: Principles, Design, Artifacts and Recent Advances, SPIE 2003, p. 7.

[ImJ] ImageJ 1.42q, http://rsbweb.nih.gov/ij/

[Kac08] Kachelrieß M., Micro-CT, Molecular Imaging I, Handbook of Experimental Pharmacology 185/I, pp.32-34, Springer, 2008.

[Ket01] Ketcham R., Carlson W., Acquisition, optimization and interpretation of X-ray computed tomographic imaginery: applications to the geosciences, Comp. Geosc. 27, pp. 381-400, 2001.

[MAV] Fraunhofer ITWM MAVI 1.3.1, http://www.itwm.fhg.de/bv/projects/MAVI/index_en.php

[Mor00] Morse B., Brigham Young University lecture, http://homepages.inf.ed.ac.uk/rbf/CVonline/LOCAL_COPIES/MORSE/threshold.pdf, 2000.

[Nar09] Narsilio G., Buzzi O., Fityus S., Yun T. S., Smith D., Upscaling of Navier-Stokes equations in porous media: Theoretical, numerical and experimental approach, Comp. Geotechnics 39, pp. 1200-1206, Elsevier, 2009.

[Rec08] Recur B., Desbarats P., Domenger J.-P., Radon and Mojette Projections Equivalence for Tomographic Reconstrucion Linear Systems, WCSG's 2008.

[Sal03] Salvato J., Nemerow N., Agardy F., Enviromental Engineering, chapter Water Quantity and Quality, pp. 267-269, John Wiley & Sons, 2003.